Editors' Suggestion

Helimagnetism in the candidate ferroelectric CrI_2

John A. Schneeloch,[1] Shunshun Liu,[2] Prasanna V. Balachandran,[2,3] Qiang Zhang,[4] and Despina Louca[1,*]

[1]*Department of Physics, University of Virginia, Charlottesville, Virginia 22904, USA*

[2]*Department of Materials Science and Engineering, University of Virginia, Charlottesville, Virginia 22904, USA*

[3]*Department of Mechanical and Aerospace Engineering, University of Virginia, Charlottesville, Virginia 22904, USA*

[4]*Neutron Scattering Division, Oak Ridge National Laboratory, Oak Ridge, Tennessee 37831, USA*

(Received 31 October 2023; revised 18 March 2024; accepted 20 March 2024; published 3 April 2024)

CrI_2 is a van der Waals layered material that exhibits helimagnetism that propagates along ribbon chains. This is determined from neutron time-of-flight diffraction measurements. Below $T_N = 17$ K in the orthorhombic structure, a screwlike helimagnetic order develops with an incommensurate wave vector of $\mathbf{q} \approx (0.2492, 0, 0)$ at 8 K. Using density functional theory (DFT) $+ U$ calculations, the J_1-J_2 model is leveraged to describe the helimagnetism, where $J_1(> 0)$ and $J_2(< 0)$ correspond, respectively, to a ferromagnetic nearest-neighbor and antiferromagnetic next-nearest-neighbor intrachain interaction. The DFT $+ U$ calculations suggest that orthorhombic CrI_2 satisfies conditions that favor formation of helimagnetic order.

DOI: 10.1103/PhysRevB.109.144403

I. INTRODUCTION

van der Waals (vdW) layered materials have a broad range of potential applications, especially when magnetic order can be manipulated [1]. Efforts in this direction surged after reports of ferromagnetic (FM) order in monolayer CrI_3 [2], antiferromagnetic (AFM) order in monolayer $FePS_3$ [3,4], and the discovery that CrI_3 can be AFM or FM depending on layer stacking [5,6]. One vdW-layered magnetic material, CrI_2, has received little attention even though its ribbon chain structure (Fig. 1) offers a new view into the nature of exchange interactions in vdW heterostructures.

CrI_2 has two polytypes with the same intralayer structure: a monoclinic phase, where the layers are oriented in the same direction [8], and an orthorhombic phase, where the layers are oriented in alternating directions [9–12], the latter being reminiscent of the T_d phase of $MoTe_2$ or WTe_2 [13]. The intralayer structure consists of a triangular lattice of Cr^{2+} ions, each surrounded by six I^- ions in an octahedral configuration, but with a Jahn-Teller (JT) distortion [10] lengthening two of these bonds so that edge-sharing octahedra form "ribbon chains" along the a axis [Figs. 1(a) and 1(b)]. The JT distortion induces a similar ribbon-chain structure in many other compounds, including $CuBr_2$ [14] and $CuCl_2$ [15], which are isostructural to monoclinic CrI_2, as well as $CrBr_2$ (which has a different layer stacking) [16], $CrCl_2$ (in which the ribbon chains do not form CrI_2-like layers) [17], and α-$PdCl_2$ [18,19].

The magnetic properties of CrI_2 are largely unexplored, with the sole attempt, to our knowledge, being a Mössbauer spectroscopy study indicating a magnetic splitting of spectral lines at 4.2 K, but not at 77 K [20]; a transition at 45(2) K was claimed, but without supporting data, and magnetic susceptibility was attempted but deemed inconclusive due to suspected contamination from the ferromagnetic CrI_3. Despite the paucity of bulk experimental studies of CrI_2, there have been three recent studies on monolayers synthesized by molecular beam epitaxy [21–23], with scanning tunneling spectroscopy showing band gaps of about 3.0 to 3.2 eV [21,22]. Several recent theoretical studies have also been reported [24–28], focusing mainly on the monolayer. In calculations, both FM [22] and AFM [28] orders result in the lowest free energy, though incommensurate ordering was not considered. Recent reports suggested that the orthorhombic phase has an out-of-plane polarization that can be reversed by sliding the layers [28]; such multiferroic behavior could lead to significant technological applications. Thus there is a clear need for experimental measurements to clarify the magnetic structure of this compound.

We report time-of-flight neutron diffraction measurements on a predominantly orthorhombic CrI_2 powder sample. Helimagnetic order is observed with a modulation wave vector $\mathbf{q} = (\delta, 0, 0)$ arising below $T_N = 17$ K with $\delta \approx 0.2492$ at 8 K and decreasing slightly on warming. DFT $+ U$ calculations were performed to estimate the exchange interactions, resulting in a sizable next-nearest-neighbor AFM intrachain coupling that suggests an origin for the helimagnetic ordering.

II. METHODS

A. Density functional theory

First-principles calculations were performed based on density functional theory (DFT) as implemented in the open-source plane-wave pseudopotential code, QUANTUM ESPRESSO [29,30]. We chose the generalized gradient approximation (GGA) and PBEsol exchange-correlation functional for all ground-state calculations [31,32]. A DFT $+ U$ approach with a Hubbard $U = 3$ eV [26] was applied on

*Corresponding author: louca@virginia.edu

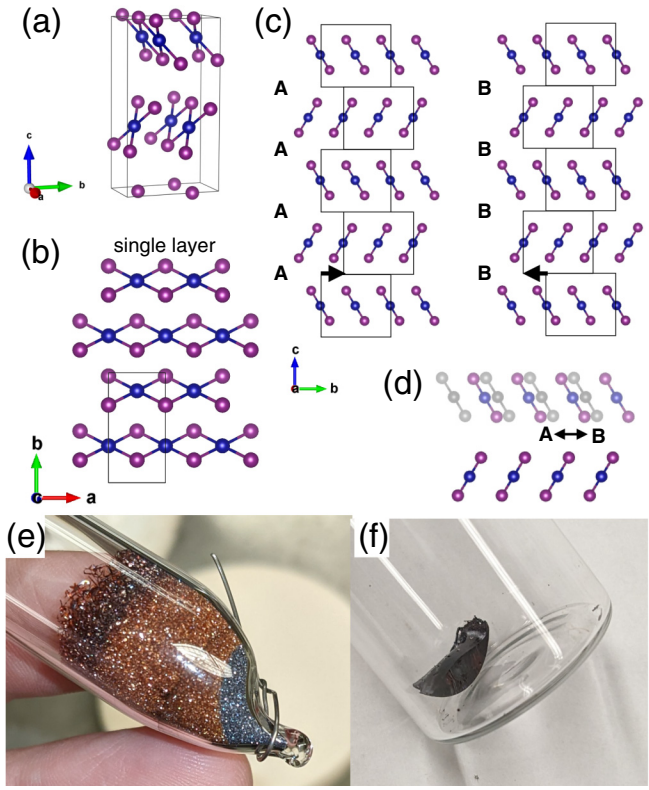

FIG. 1. (a) Crystal structure of orthorhombic CrI_2, showing ribbon chains along the *a* axis. (b) One layer of CrI_2 in the *ab* plane. (c) Both twins of orthorhombic CrI_2 depicted in the *bc* plane, constructed by A- and B-type stacking, respectively. (d) An illustration that A- and B-type stacking are related by translations along the *b* axis. (e) Photo of a CrI_2 synthesis attempt, in which the ampoule (with stoichiometric Cr and I) was hung in a vertical tube furnace at 600 °C. The boundary between the silvery (CrI_3) and red (CrI_2) powder suggests the influence of a temperature gradient, where CrI_3 formed in a slightly cooler region of the ampoule. The outer diameter of the ampoule was 23 mm. (f) Photo of a 0.5 g melt-grown piece of CrI_2, in a vial of outer diameter 24 mm. Crystal structures plotted using VESTA [7].

the Cr-3*d* orbitals to account for the correlated orbital effects [33,34]. The kinetic energy cutoff was set to 70 Ry for the wave functions and the Brillouin zone was sampled using a Γ-centered Monkhorst-Pack *k* mesh for all calculations [35]. A semiempirical Grimme DFT-D3 vdW dispersion correction approach with three-body contribution was also applied to treat the vdW bonding in the CrI_2 crystal [36]. We used the orthorhombic crystal structure (space group no. 36, $Cmc2_1$) for our DFT + *U* calculation. In this space group, there are two unique crystallographic sites for the I atoms, whereas there is only one unique site for the Cr atoms. All atoms occupy the Wyckoff site labeled "4a." We performed full crystal structure relaxation (with and without the vdW dispersion correction) where both the unit cell parameters and atomic coordinates are relaxed. Convergence thresholds for the maximum residual force and maximum energy difference between consecutive iterations were set at less than 1.5×10^{-5} a.u. and 7×10^{-10} Ry, respectively. Representative unit cells of DFT + *U* relaxed CrI_2 crystal structures are given in Fig. S4. The atomic parameters of the DFT + *U* relaxed crystal structures with and without the vdW dispersion correction are in the CIF files included in the Supplemental Material [37]. The DFT + *U* calculated absolute Cr magnetic moment is determined to be $\sim 3.79 \mu_B$, regardless of the specific spin configuration.

We employed the methodology introduced by Banks *et al.* [38] to compute the spin-exchange parameters, J_n. We constructed a $4 \times 1 \times 1$ supercell and considered six independent collinear spin arrangements (one FM and five AFM, which are shown in Fig. S5). We then performed self-consistent field calculations using a Γ-centered *k* mesh of $4 \times 7 \times 4$. The total energy data, along with the Heisenberg Hamiltonian used to calculate each *J* from the supercell, is given in Sec. VI in the Supplemental Material [37].

B. Experimental details

CrI_2 powder was synthesized by sealing a stoichiometric mixture of fine (−200 mesh) chromium powder and iodine pieces in ampoules and heating to 650 °C within a day, then staying at 650 °C or 750 °C for several days before furnace cooling. Below ∼600 °C, CrI_3 forms instead, and an ampoule heated at 600 °C in a vertical tube furnace showed a sharp divide between silvery CrI_3 and red CrI_2 powder [Fig. 1(e)], due to CrI_3 forming in the cooler region of the temperature gradient. For the single crystals used for the magnetic susceptibility, CrI_2 crystals were grown from a melt by heating an ampoule with a stoichiometric mixture of Cr and I up to 900 °C, then furnace cooling to 750 °C before quenching in water. Slow cooling from 900 °C to 750 °C resulted in larger crystals, such as the 0.5 g piece shown in Fig. 1(f). (The melting temperature is 867 °C [11].) CrI_2 is hygroscopic and crystals disintegrate within minutes in humid air, though they can be stored in dry air for weeks without visible deterioration.

Neutron diffraction experiments were performed on the POWGEN diffractometer at the Spallation Neutron Source of Oak Ridge National Laboratory [39]. The powder was loaded into a vanadium can in a helium glovebox before measurement. A POWGEN automatic changer was adopted as the sample environment. Two neutron banks with center wavelengths of 1.5 Å and 2.665 Å were used for the data collection. Refinement was done using calculations in which the diffuse scattering was obtained from the formalism of Ref. [40]; the software GSAS-II [41] was used to obtain lattice parameters. Single crystal x-ray measurements were also carried out as a function of temperature, with data refined using the software APEX4 by Bruker.

III. RESULTS

A. Single-crystal x-ray diffraction

Single-crystal x-ray diffraction (SCXRD) on a vapor-tranport grown crystal was performed as a function of temperature. An intensity plot in the (0*KL*) scattering plane at 100 K is shown in Fig. 2(a). The refined lattice and atomic parameters are shown in Tables I and II, respectively. From Fig. 2(a), not only is the main (orthorhombic) phase observed, but also a secondary, coaligned phase with the monoclinic structure [8] (with two Bragg peaks indicated by arrows), as well as diffuse scattering streaks indicating some degree of

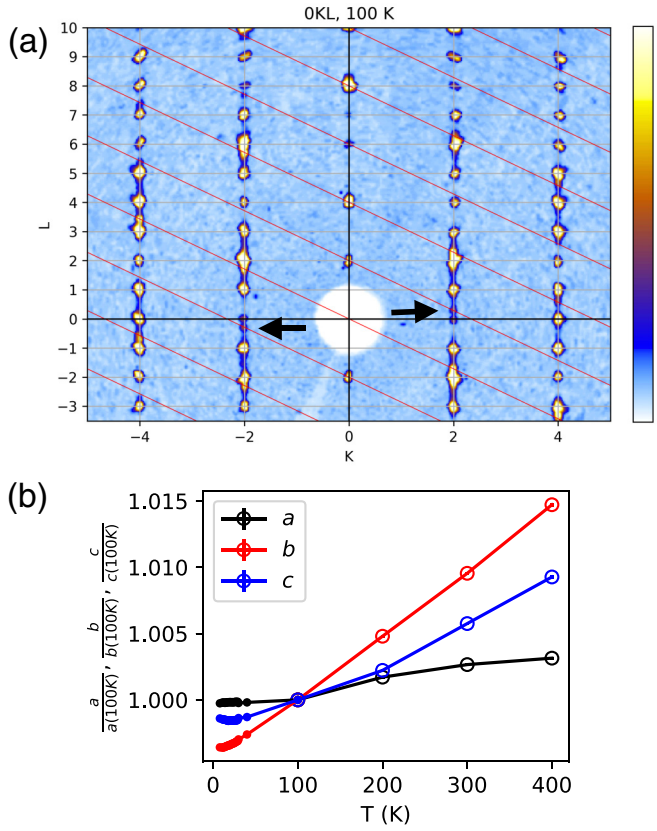

FIG. 2. (a) Single-crystal x-ray diffraction (SCXRD) intensity in the 0KL plane. In addition to the orthorhombic phase peaks, additional peaks from the monoclinic polytype [8] are seen, with two monoclinic peaks indicated by arrows. The gray grid lines and the labels on the axes correspond to the orthorhombic phase. The red lines show the monoclinic-phase $(H0L)_M$ lines for integer L; $K_{\text{orth}} = H_{\text{mono}}$ and $L_{\text{orth}} = 2(L_{\text{mono}} - \epsilon H_{\text{mono}})$, with $\epsilon \approx 0.43$. Both phases share the same vertical axis. (b) Lattice parameters plotted vs temperature, normalized to their 100 K values. Open circles denote SCXRD values, measured for $T \geqslant 100$ K, and dots denote neutron diffraction values, measured for $T \leqslant 100$ K.

stacking disorder. No sign of a structural phase transition was observed from 100 to 400 K. A crystal from a melt-grown batch was also measured by SCXRD and verified to have the orthorhombic structure. The temperature dependence of the lattice parameters (from the SCXRD and neutron diffraction data) are plotted in Fig. 2(b). The thermal expansion is smallest along the a axis, which is as expected given the stronger bonding along the chains (as seen in structurally similar $CuCl_2$ [38]).

TABLE I. Lattice parameters from SCXRD refinement.

	100 K	200 K	300 K	400 K
a (Å)	3.9070(5)	3.9158(3)	3.9195(3)	3.9214(4)
b (Å)	7.4963(17)	7.5366(8)	7.5722(6)	7.6110(10)
c (Å)	13.479(3)	13.5142(13)	13.5618(10)	13.6092(17)

TABLE II. Atomic positions from SCXRD refinement. Lattice parameters are shown in Table I. The space group is $Cmc2_1$. All Wyckoff symbols are "4a."

	x	y	z	U_{iso}
100 K				
I1	0	0.2045(3)	0.37815(17)	0.0108(8)
I2	0	0.4720(3)	0.62193(11)	0.0115(8)
Cr1	0.5	0.3377(9)	0.4987(6)	0.0128(14)
200 K				
I1	0	0.20577(8)	0.37850(4)	0.01277(17)
I2	0	0.47094(8)	0.62147(3)	0.01374(18)
Cr1	0.5	0.3379(3)	0.49992(15)	0.0156(3)
300 K				
I1	0	0.20706(10)	0.37872(5)	0.01927(19)
I2	0	0.47003(9)	0.62127(3)	0.02039(19)
Cr1	0.5	0.3383(3)	0.49975(17)	0.0227(4)
400 K				
I1	0	0.20813(16)	0.37891(8)	0.0270(3)
I2	0	0.46917(16)	0.62096(5)	0.0279(3)
Cr1	0.5	0.3378(5)	0.5000(3)	0.0309(7)

B. Powder neutron diffraction

Figures 3(a) and 3(b) are a plot of the neutron diffraction data collected at two temperatures, 8 and 30 K. A substantial amount of diffuse scattering arising from stacking disorder is observed, which is accounted for in the calculated curves and will be discussed below. Selected nuclear and magnetic Bragg peaks are labeled in Figs. 3(a) and 3(b); a more comprehensive indexing can be found in Fig. S1 of the Supplemental Material [37], along with the expected intensity in the absence of stacking disorder. At 30 K, almost every peak can be indexed by the orthorhombic (ortho-CrI_2) structure [10]. Only one small peak above $d = 2.0$ Å (at $d = 2.81$ Å) is inconsistent with the ortho-CrI_2 structure; this peak is likely the (111) peak of the monoclinic CrI_2 polytype [8], which would imply a volume ratio of about 1% relative to the orthorhombic phase if we assume no monoclinic-phase stacking disorder. Little change in intensity is seen from 30 to 40 K or 100 K [Fig. 3(c)]. No sign of CrI_3 was observed, in either the $R\bar{3}$ or $C2/m$ phases [6]. Some preferred orientation was present, as seen in the ratio of peaks such as (200) and (00L) ($L = 2, 4, 6$), whose intensities would be immune to stacking disorder. We found a March-Dollase ratio of 1.15 to be satisfactory in our calculations [42].

The diffuse scattering arises from a disordered sequence of the two stacking options present in the orthorhombic CrI_2 crystal structure [Figs. 1(c) and 1(d)]. Using the same notation as for similar stacking variations seen in $Mo_{1-x}W_xTe_2$ [43], we can construct one ortho-CrI_2 twin by a repeated "A"-type stacking operation. Since each layer has approximate inversion symmetry, an inversion operation keeps the intralayer structure largely unchanged but changes the layer stacking from A type to "B" type, related by alternating b-axis translations of about ± 0.344 lattice units. Calculations of the diffuse scattering were performed using the formalism of Ref. [40], which is the basis for the software DIFFAX; see the Supplemental Material for mathematical details [37]. For our data,

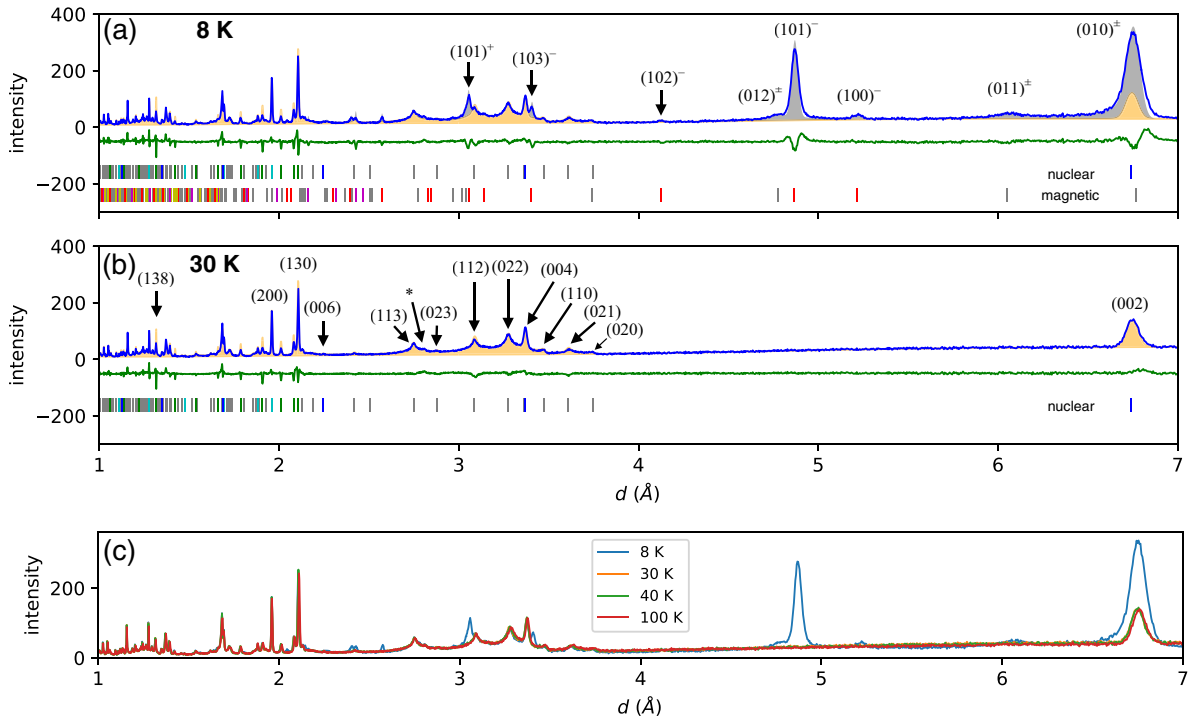

FIG. 3. (a), (b) Neutron diffraction intensity (blue curves) at (a) 8 K and (b) 30 K, compared to calculated intensity from the model described in the text, shaded orange and gray for nuclear and magnetic intensity, respectively. The green curve is the difference between the data and the calculation. The locations of nuclear and magnetic peaks (with $+/-/\pm$ superscripts omitted) are indicated below the data, colored blue for $(00L)$, magenta for $(03L)$, red for $(10L)$, green for $(13L)$, cyan for $(20L)$, yellow for $(23L)$, and gray for the remaining peaks. Selected peaks are labeled. The asterisk (*) denotes the possible (111) peak of the monoclinic polytype. (c) Neutron diffraction data at 8, 30, 40, and 100 K. No peaks were present above $d = 7$ Å.

we find satisfactory agreement if we assume the intensity is the sum of two contributions with 22% of (nearly ordered) $p = 0.05$ and 78% of (random) $p = 0.5$, where p is the probability of switching stacking types (from A to B type or vice versa) between consecutive layers. Certain peaks are expected to be unaffected by stacking disorder, in particular, (HKL), where K is a small multiple of 3. This invariance is due to the stacking translations randomly contributing phases of $\exp(\pm 2\pi i K \times 0.344)$ to terms in the summation of the structure factor, which are about unity when K is a small multiple of 3. The $(H0L)$ peaks are certainly prominent in our data. The $(13L)$ peaks, though, while prominent, are substantially weaker than expected from our calculations [e.g., (138) in Fig. 3(b)]. A likely possibility is the presence of additional types of stacking, such as those in monoclinic CrI_2 [8] or $CrBr_2$ [16]; preliminary calculations suggest that such stacking may be (randomly) present on the order of 10–20%, but an in-depth calculation is beyond the scope of this paper.

Below 17 K, magnetic satellite peaks appear at $(H \pm \delta, K, L)$ for odd $H + K$, with $\delta \approx 0.248$. The peaks are labeled $(HKL)^+$, $(HKL)^-$, or $(0KL)^\pm$. We performed representation analysis of the possible magnetic structures using the software SARAh, as discussed in Sec. III of the Supplemental Material [37]. The spin structure that best describes our data consists of screwlike helimagnetism propagating along the ribbon chains, with the spins rotating in the bc plane and in the same direction between layers. We can envision the spin structure by starting with the arrangement depicted in Fig. 4(a), which has (1) intralayer AFM order and (2) nearly AFM alignment (a phase difference of $\sim 210°$) between spins at position $x = 0$ along the ribbon chain axis. Next, we apply a helical twist of $\sim 90° x$ to arrive at the spin structure that is consistent with our data. (An equivalent picture, discussed in the Supplemental Material [37], is to start with spins FM aligned within each layer, then apply a twist of $\sim 450° x$; for this picture, the propagation vector would be $\mathbf{k} = (1 + \delta, 0, 0)$ and the peaks would be located at $[H \pm (1 + \delta), K, L]$ for even $H + K$.) The intralayer AFM in the pre-"twisted" spin structure is responsible for peaks being present only at odd $H + K$. The $\sim 210°$ phase difference between the layers (specifically, the fact that it is not 180°) is responsible for the small but nonzero intensity of $(100)^-$. The pretwisted spin structure resembles that predicted in Ref. [28], though the helical modulation was not in that proposed structure. Two chiralities are possible for the proposed spin structure, though even with single-crystal neutron scattering, we would be unable to distinguish these domains with unpolarized neutrons.

The magnetic peaks are affected by stacking disorder in the same way as the nuclear peaks, i.e., peaks with $K = 0$ remain prominent, peaks with $K = 3$ are diminished relative to calculations but still prominent, and the remaining peaks are typically greatly broadened. The similar broadening for nuclear and magnetic peaks suggests that only the *locations* of the spins are disordered (due to random stacking translations), while disorder in the *orientation* of the spins is not needed to explain our data.

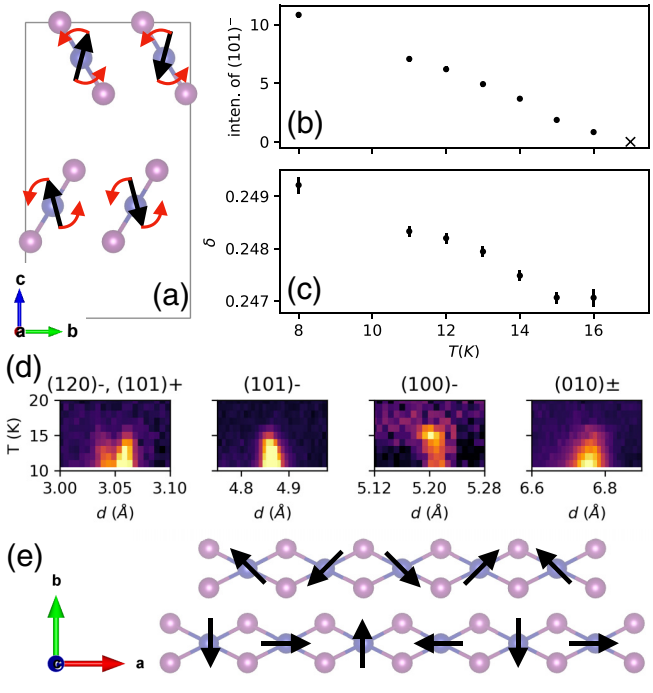

FIG. 4. (a) Depiction of the proposed "untwisted" spin structure in the *bc* plane, i.e., the orientation of the spins before applying the helimagnetic spin rotation along the chain direction. (b), (c) The temperature dependence of (b) the intensity of the magnetic $(101)^-$ peak [divided by the intensity of (200)] and (c) the magnitude of the modulation vector $(\delta, 0, 0)$. The "X" in (b) denotes zero intensity. (d) Magnetic intensity near selected peaks, obtained from the 11 to 20 K data by subtracting a background of the average intensity from 20 to 29 K. (e) Depiction of helical spin rotation along the *a* axis for a pair of neighboring ribbon chains within a layer. For visual clarity, these spins are depicted rotating normal to the layers, but the helical plane determined from our data is *bc*.

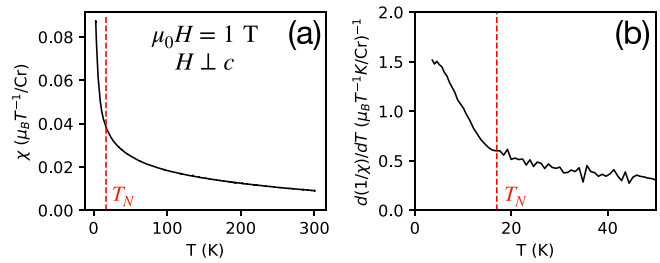

FIG. 5. (a) Magnetic susceptibility of a melt-grown CrI_2 crystal with a 1 T magnetic field applied in-plane. (b) The derivative $d(1/\chi)/dT$ for the data in (a). $T_N = 17$ K is depicted as a red dashed line.

While magnetic ordering increases on cooling, the ordered magnetic moment is not close to saturation down to 8 K, as seen from the intensity of the magnetic $(101)^-$ peak in Fig. 4(b). A refinement (see Supplemental Material for details [37]) resulted in an ordered magnetic moment of $2.95(10)\mu_B/Cr^{2+}$ ion. This value is well short of the $4\mu_B/Cr^{2+}$ expected for the high-spin Cr^{2+} values of $g = 2$ and $S = 2$. The magnitude of the modulation vector $(\delta, 0, 0)$ is plotted in Fig. 4(c); δ was obtained by fitting the positions of the $(120)^-$, $(101)^-$, $(101)^+$, $(100)^-$, $(103)^+$, and $(103)^-$ peaks, all but $(120)^-$ which should be unaffected by stacking disorder. Though $\delta \approx 1/4$, the modulation vector is incommensurate, with δ decreasing from ~0.2492 to ~0.2470 on warming from 8 to 16 K. These values correspond to rotations of spins between consecutive Cr^{2+} ions along the ribbon chains of 89.7° and 88.9°.

What effect does the stacking disorder have on the magnetic order? On the one hand, we expect significant interlayer coupling, as was seen for structurally similar CrI_3 (with a value of −0.59 meV for the summed exchange constants for interlayer bonding for the $R\bar{3}$ phase [44]). Our DFT calculations (to be discussed below) also suggest a sizable interlayer magnetic coupling. However, for symmetry reasons, we expect the magnetic ordering to be largely unaffected by the A/B stacking disorder. If we apply an inversion operation to one twin of the structure, which we call "AA" to denote its A-type stacking, we end up with the "BB" twin. However, spin is a pseudovector and does not change its orientation upon inversion. Inversion about a particular layer would simply swap the spins of layers of equal distance above and below that layer, which would do nothing in a system like CrI_2 where the spin direction repeats every two layers. The same spin structure would, thus, be valid for both the AA and BB twins. Assuming that magnetic interactions beyond nearest neighboring layers are negligible, the relative spin orientation of neighboring layers should, then, be independent of A- or B-type stacking and no disorder in the orientation of the magnetic moments should arise from the A/B stacking disorder. This situation is different from that in CrI_3, where the different types of stacking (monoclinic and rhombohedral) are not symmetry equivalent and a stacking dependence of the spin orientation is observed [6]. We note, though, that partial layer sliding, such as during coherent phonon oscillations produced in ultrafast pump-probe spectroscopy [45], could modulate the interlayer magnetic coupling and thus the relative phase of the spin helices of neighboring layers.

C. Magnetic susceptibility

The onset of helimagnetic order can also be inferred from magnetization data taken on melt-grown crystals, suggesting that the magnetic transition temperature is only weakly affected by stacking disorder. The magnetic susceptibility has a monotonic increase on cooling [Fig. 5(a)]. This behavior contrasts with the broad hump often seen in quasi-one-dimensional magnetic systems, with the most relevant examples being $CrCl_2$ [46], $CuCl_2$ [38], and $CuBr_2$ [47,48], suggesting the role of stronger interlayer and interchain interactions in CrI_2. The inverse magnetization is roughly linear above $T_N \sim 17$ K, with a fit resulting in a Curie-Weiss temperature of about −70 K [see Fig. S3(a) in the Supplemental Material [37]], suggesting the dominance of antiferromagnetic interactions. Below T_N, though, the derivative $d(1/\chi)/dT$ shows a marked upturn, indicating the onset of helimagnetic ordering [Fig. 5(b)]. Magnetization vs field at 3 K [Fig. S3(b)] shows linear and nonhysteretic behavior at low fields, with a possible transition induced by fields above ~3 T. Generally, we saw similar behavior for magnetic field

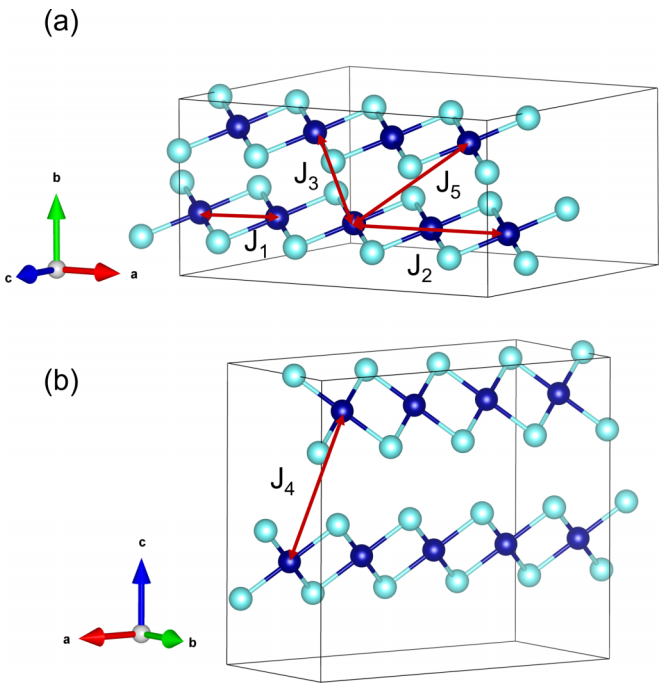

FIG. 6. Definition of J_n of CrI_2 supercell. The dark blue color represents Cr atoms and the cyan color corresponds to I atoms. (a) J_1 and J_2 is nearest- and next-nearest-neighbor intrachain Cr-Cr interaction. J_3 and J_5 is nearest- and next-nearest-neighbor intralayer interchain Cr-Cr interaction. (b) J_4 is nearest-neighbor interlayer Cr-Cr interaction.

applied in-plane or out-of-plane, but further study is needed to determine the extent to which in-plane anisotropy is present, i.e., along or perpendicular to the ribbon chains.

D. Density functional theory calculations

To determine whether or not the helimagnetism of CrI_2 has a similar origin as for the intrachain frustrated magnetic interactions in CuX_2 (X = Cl, Br), we performed DFT + U calculations using crystal structures that were relaxed with and without the vdW dispersion correction. We computed the energies of a number of collinear spin configurations, then mapped their relative energies to the following spin Hamiltonian

$$H = \sum_{i<j} -J_{ij}\hat{\mathbf{S}}_i \cdot \hat{\mathbf{S}}_j \qquad (1)$$

to obtain the exchange interactions J_n (our definition of J_1–J_5 is shown in Fig. 6). In terms of differences in the DFT + U relaxed crystal structures, introduction of vdW dispersion correction has an impact on the unit cell volume. The crystal structure with vdW correction had a smaller unit cell volume (385 Å^3) when compared to the crystal structure without the vdW dispersion correction (404 Å^3). As a result, introduction of vdW correction reduced the Cr-Cr bond lengths leading to closer intrachain and interlayer bond distances (see Table III).

The DFT + U derived exchange interactions for coordinates relaxed with or without the vdW correction are shown in Table III. The total energy difference data used for the calculation of J_n is given in Table S1. As shown in Fig. 6, the terms J_1 and J_2 correspond to exchange energies that arise due to the nearest- and next-nearest-neighbor intrachain Cr-Cr bonds.

TABLE III. Exchange interactions per Cr-Cr bond from DFT + U calculations (U = 3 eV) using crystal structures that were relaxed with and without vdW correction. $J_n < 0$ indicates favoring AFM exchange coupling.

Relaxation procedure	Cr-Cr (Å)	J_n (meV)
DFT+U+vdW relaxed	3.930	$J_1 = 2.99$
	7.861	$J_2 = -2.19$
	4.196	$J_3 = -0.42$
	7.017	$J_4 = 2.11$
	6.965	$J_5 = 0.03$
DFT+U relaxed	3.947	$J_1 = 3.55$
	7.894	$J_2 = -2.14$
	4.279	$J_3 = -0.27$
	7.195	$J_4 = 1.36$
	7.033	$J_5 = 0.03$

A simple model for helimagnetism is the J_1-J_2 model [49], where spins on a one-dimensional chain are coupled with nearest-neighbor J_1 and next-nearest-neighbor J_2 exchange constants. In this model, helimagnetism results if J_2 is AFM ($J_2 > 0$) and $|J_2| > |J_1|/4$. In the limit of large J_2, the twist angle between neighboring spins is 90°. From Table III, our DFT-calculated J_1 and J_2 values satisfy the J_1-J_2 model condition, providing an indication that the sizably AFM J_2 constant may be responsible for the helimagnetism in CrI_2. Of course, additional coupling constants are present and, with all of the interactions, the energy of the Heisenberg model is minimized for a twist angle of about 60° per Cr ion along the ribbon chains, substantially off from ∼90°. Thus more detailed calculations are needed to get a better understanding of the microscopic interactions in CrI_2 and should include aspects such as spin-orbit coupling and noncollinear spins. Regardless, our DFT calculations suggest that a substantially AFM next-nearest-neighbor coupling is a plausible explanation for the helimagnetism. Additionally, from the magnitude of J_4, we see that interlayer magnetic coupling is non-negligible and cannot be ignored.

IV. DISCUSSION

There are striking similarities in both the structure and magnetism between CrI_2 and CuX_2 (X = Cl, Br), as well as many other Cu^{2+} ribbon-chain compounds. Aside from differences in layer stacking, CuX_2 (X = Cl, Br) is isostructural to CrX_2 (X = Br, I), with JT distortions of the $Cu^{2+}X_6^-$ and $Cr^{2+}X_6^-$ octahedra resulting in ribbon-chain structures. Helimagnetic order has been reported in $CuCl_2$ below 24 K [38] and in $CuBr_2$ below 73.5 K [47], with both exhibiting ∼90° rotations of spins along the chain axis between consecutive Cu/Cr ions (specifically, 81° for $CuCl_2$ and 85° for $CuBr_2$) and an antiferromagnetism between intralayer chains similar to CrI_2. One difference, though, is the plane of the helical rotation; $CuCl_2$ and $CuBr_2$ are reported to have

spins rotate cycloidally within the plane that includes the chain and out-of-plane directions, whereas the spins in orthorhombic CrI_2 appear to rotate perpendicular to the chain. A number of other Cu^{2+} ribbon-chain compounds also exhibit helimagnetism, such as $LiCuVO_4$ [50,51], $LiCu_2O_2$ [52], $NaCuMoO_4(OH)$ [53], and $PbCuSO_4(OH)_2$ [54]. The helimagnetism is often described in terms of the J_1-J_2 model. It is frequently assumed that the helimagnetism in the Cu^{2+} ribbon chain compounds arises from the frustration between an AFM J_2 and a sufficiently weak J_1, though there are disagreements as to whether the J_1-J_2 model can fully explain the magnetism or where different materials fall in regards to the size of the $|J_1/J_2|$ ratio. While there has been plenty of research into the helimagnetism of Cu^{2+} compounds, few such studies have been done of their Cr^{2+} counterparts. ($CrCl_2$ is an exception; though collinear AFM ordering sets in below 16 K [55] or 11.3 K [56], depending on the polymorph, intriguingly, short-range helimagnetic order has been reported [56], with a $\sim 97^\circ$ rotation angle between neighboring spins.) The case of CrI_2 suggests a similarity in the magnetism of Cr^{2+} and Cu^{2+} ribbon chain compounds that should be explored further.

A better understanding of the connection between the helimagnetism and ribbon-chain structure of CrI_2 could be achieved by (1) measuring the magnetic behavior of $CrBr_2$, which is, thus far, unreported, (2) performing a more detailed study on the short-range helimagnetism of $CrCl_2$, and (3) conducting inelastic neutron scattering measurements on CrI_2 to validate the exchange interactions between the ions, paired with more in-depth DFT + U calculations that go beyond collinear spin structures and include the effects of spin-orbit coupling.

The helimagnetism of CrI_2 presents a number of opportunities for future research. There is the potential for sliding ferroelectricity in orthorhombic CrI_2 by virtue of its layer stacking [28], in which the electric polarization may be switchable via layer sliding as has been observed for other bilayer systems such as WTe_2 and hexagonal boron nitride [57]. Another research opportunity involves the search for a monolayer helimagnetic multiferroic. NiI_2 has recently gained attention for being a potential single-layer multiferroic [58], where the ferroelectricity (FE) is assumed to arise from the helimagnetic ordering [59] (though there is controversy as to whether FE has, in fact, been demonstrated [60]). We have shown that CrI_2 is helimagnetic in the bulk and isolation of monolayers of CrI_2 has already been reported [21–23], so monolayer CrI_2 would be a natural candidate for helimagnetism. We should make a couple of points, however. First, while (nearly isostructural) $CuBr_2$ was reported to have strong magnetoelectric coupling associated with its helimagnetic ordering [47], the spin helix is cycloidal in $CuBr_2$ and CrI_2, but screwlike in CrI_2, and only cycloidal helices are expected to generate a ferroelectric polarization by the inverse Dzyaloshinskii-Moriya mechanism [59]. However, an applied magnetic field may change the helical plane and allow (or suppress) FE, as has been demonstrated for $CuCl_2$ [61]. Second, the magnetic order for monolayer CrI_2 may differ from that of the bulk; the helimagnetism in monolayer NiI_2, in fact, has been reported to have a different wave vector than bulk NiI_2 [62]. An investigation into the magnetic properties of monolayer CrI_2 would, no doubt, enlighten the search for novel magnetic materials in the few-layer limit.

V. CONCLUSION

In conclusion, we observed via neutron diffraction the onset of helimagnetic order below 17 K in orthorhombic CrI_2. The spin helix propagates along the chain direction with a wave vector of about (0.2492,0,0) at 8 K, decreasing slightly in magnitude on warming. Our DFT + U calculations provide evidence suggesting that one of the key factors behind the helimagnetism may be a sizable antiferromagnetic next-nearest-neighbor intrachain coupling.

ACKNOWLEDGMENTS

The work at the University of Virginia is supported by the Department of Energy, Grant No. DE-FG02-01ER45927. The Spallation Neutron Source is a DOE Office of Science User Facility operated by Oak Ridge National Laboratory.

[1] M. A. McGuire, Cleavable magnetic materials from van der Waals layered transition metal halides and chalcogenides, J. Appl. Phys. **128**, 110901 (2020).

[2] B. Huang, G. Clark, E. Navarro-Moratalla, D. R. Klein, R. Cheng, K. L. Seyler, D. Zhong, E. Schmidgall, M. A. McGuire, D. H. Cobden, W. Yao, D. Xiao, P. Jarillo-Herrero, and X. Xu, Layer-dependent ferromagnetism in a van der Waals crystal down to the monolayer limit, Nature (London) **546**, 270 (2017).

[3] J.-U. Lee, S. Lee, J. H. Ryoo, S. Kang, T. Y. Kim, P. Kim, C.-H. Park, J.-G. Park, and H. Cheong, Ising-type magnetic ordering in atomically thin $FePS_3$, Nano Lett. **16**, 7433 (2016).

[4] X. Wang, K. Du, Yu Yang Fredrik Liu, P. Hu, J. Zhang, Q. Zhang, M. H. S. Owen, X. Lu, C. K. Gan, P. Sengupta, C. Kloc, and Q. Xiong, Raman spectroscopy of atomically thin two-dimensional magnetic iron phosphorus trisulfide ($FePS_3$) crystals, 2D Mater. **3**, 031009 (2016).

[5] B. Huang, M. A. McGuire, A. F. May, D. Xiao, P. Jarillo-Herrero, and X. Xu, Emergent phenomena and proximity effects in two-dimensional magnets and heterostructures, Nat. Mater. **19**, 1276 (2020).

[6] J. A. Schneeloch, L. Daemen, and D. Louca, Antiferromagnetic-ferromagnetic homostructures with Dirac magnons in the van der Waals magnet CrI_3, Phys. Rev. B **109**, 024409 (2024).

[7] K. Momma and F. Izumi, *VESTA* 3 for three-dimensional visualization of crystal, volumetric and morphology data, J. Appl. Cryst. **44**, 1272 (2011).

[8] J. W. Tracy, N. W. Gregory, J. M. Stewart, and E. C. Lingafelter, The crystal structure of chromium(II) iodide, Acta Cryst. **15**, 460 (1962).

[9] L. Guen, M. Alléaume, R. Éholié, J. Flahaut, and G. Chaudron, Étude du systéme chrome-iode, C. r. Acad. Sci., C **275**, 111 (1972).

[10] F. Besrest and S. Jaulmes, Structure cristalline de l'iodure de chrome, CrI_2, Acta Cryst. **29**, 1560 (1973).

[11] L. Guen, H. D. Nguyen, R. Éholie, and J. Flahaut, Systémes CrI_2-MI_2 (M = Ti, V, Mn, Fe, Co, Ni, Zn) Diagrammes de Phases, Étude Structurale Effet Jahn-Teller Coopératif, Ann. Chim. **1**, 39 (1976).

[12] L. Guen and Nguyen-Huy-Dung, Manganése(II) Chrome(II) Diiodure: Phase β de (Mn,Cr)I_2, Acta Cryst. **32**, 311 (1976).

[13] R. Clarke, E. Marseglia, and H. P. Hughes, A low-temperature structural phase transition in β-$MoTe_2$, Philos. Magazine B **38**, 121 (1978).

[14] O. Oeckler and A. Simon, Redetermination of the crystal structure of copper dibromide, $CuBr_2$, Z. Kristallogr.–New Cryst. Struct. **215**, 13 (2000).

[15] A. F. Wells, 333. The crystal structure of anhydrous cupric chloride, and the stereochemistry of the cupric atom, J. Chem. Soc. **1947**, 1670 (1947).

[16] J. W. Tracy, N. W. Gregory, and E. C. Lingafelter, Crystal structure of chromium(II) bromide, Acta Cryst. **15**, 672 (1962).

[17] J. W. Tracy, N. W. Gregory, E. C. Lingafelter, J. D. Dunitz, H.-C. Mez, R. E. Rundle, C. Scheringer, H. L. Yakel, and M. K. Wilkinson, The crystal structure of chromium(II) chloride, Acta Cryst. **14**, 927 (1961).

[18] A. F. Wells, The crystal structure of palladous chloride $PdCl_2$, Z. Kristallogr.–Cryst. Mater. **100**, 189 (1939).

[19] J. Evers, W. Beck, M. Göbel, S. Jakob, P. Mayer, G. Oehlinger, M. Rotter, and T. M. Klapötke, The structures of δ-$PdCl_2$ and γ-$PdCl_2$: Phases with negative thermal expansion in one direction, Angew. Chem., Int. Ed. **49**, 5677 (2010).

[20] B. Djermouni, Structural and magnetic properties of CrI_2, CrI_3, $CsCrI_3$ and $FeSb_2O_4$ from ^{129}I and ^{121}Sb Moessbauer spectroscopy, Ph.D. thesis, L'Université Louis Pasteur de Strasbourg, France, 1976, cRN-CNPA–76-14 INIS Ref. No. 8302241.

[21] X. Cai, Z. Xu, S.-H. Ji, N. Li, and X. Chen, Molecular beam epitaxy growth of iodide thin films, Chin. Phys. B **30**, 028102 (2021).

[22] L. Peng, J. Zhao, M. Cai, G.-Y. Hua, Z.-Y. Liu, H.-N. Xia, Y. Yuan, W.-H. Zhang, G. Xu, L.-X. Zhao, Z.-W. Zhu, T. Xiang, and Y.-S. Fu, Mott phase in a van der Waals transition-metal halide at single-layer limit, Phys. Rev. Res. **2**, 023264 (2020).

[23] P. Li, N. Liu, J. Zhang, S. Chen, X. Zhou, D. Guo, C. Wang, W. Ji, and D. Zhong, Two-dimensional magnetic semiconducting heterostructures of single-layer CrI_3-CrI_2, ACS Appl. Mater. Interfaces **15**, 19574 (2023).

[24] V. V. Kulish and W. Huang, Single-layer metal halides MX_2 (X = Cl, Br, I): stability and tunable magnetism from first principles and Monte Carlo simulations, J. Mater. Chem. C **5**, 8734 (2017).

[25] J. Zhang, J. Yang, L. Lin, and J.-J. Zhu, An antiferromagnetic two-dimensional material: Chromium diiodides monolayer, J. Semicond. **41**, 122502 (2020).

[26] Y. Zhao, H. Liu, J. Gao, and J. Zhao, Transition of CrI_2 from a two-dimensional network to one-dimensional chain at the monolayer limit, Phys. Chem. Chem. Phys. **23**, 25291 (2021).

[27] L. Yang, Y. Gao, M. Wu, and P. Jena, Interfacial triferroicity in monolayer chromium dihalide, Phys. Rev. B **105**, 094101 (2022).

[28] S. Zhang, F. Tang, X. Song, and X. Zhang, Structural phase transitions and Raman identifications of the layered van der Waals magnet CrI_2, Phys. Rev. B **105**, 104105 (2022).

[29] P. Giannozzi, S. Baroni, N. Bonini, M. Calandra, R. Car, C. Cavazzoni, D. Ceresoli, Guido L Chiarotti, M. Cococcioni, I. Dabo *et al.*, QUANTUM ESPRESSO: a modular and open-source software project for quantum simulations of materials, J. Phys.: Condens. Matter **21**, 395502 (2009).

[30] P. Giannozzi, O Andreussi, T Brumme, O Bunau, M Buongiorno Nardelli, M Calandra, R Car, C Cavazzoni, D Ceresoli, M Cococcioni *et al.*, Advanced capabilities for materials modelling with QUANTUM ESPRESSO, J. Phys.: Condens. Matter **29**, 465901 (2017).

[31] J. P. Perdew, K. Burke, and M. Ernzerhof, Generalized gradient approximation made simple, Phys. Rev. Lett. **77**, 3865 (1996).

[32] J. P. Perdew, A. Ruzsinszky, G. I. Csonka, O. A. Vydrov, G. E. Scuseria, L. A. Constantin, X. Zhou, and K. Burke, Restoring the density-gradient expansion for exchange in solids and surfaces, Phys. Rev. Lett. **100**, 136406 (2008).

[33] V. I. Anisimov, J. Zaanen, and O. K. Andersen, Band theory and mott insulators: Hubbard U instead of Stoner I, Phys. Rev. B **44**, 943 (1991).

[34] I. V. Solovyev, P. H. Dederichs, and V. I. Anisimov, Corrected atomic limit in the local-density approximation and the electronic structure of d impurities in Rb, Phys. Rev. B **50**, 16861 (1994).

[35] H. J. Monkhorst and J. D. Pack, Special points for Brillouin-zone integrations, Phys. Rev. B **13**, 5188 (1976).

[36] S. Grimme, J. Antony, S. Ehrlich, and H. Krieg, A consistent and accurate *ab initio* parametrization of density functional dispersion correction (DFT-D) for the 94 elements H-Pu, J. Chem. Phys. **132**, 154104 (2010).

[37] See Supplemental Material at http://link.aps.org/supplemental/10.1103/PhysRevB.109.144403 for additional details on the computation of diffraction patterns with and without diffuse scattering, a representation analysis of the possible magnetic structures, additional magnetization data, and density functional theory calculation details. Supplement Material contains Refs. [38,40,48,63–67].

[38] M. G. Banks, R. K. Kremer, C. Hoch, A. Simon, B. Ouladdiaf, J.-M. Broto, H. Rakoto, C. Lee, and M.-H. Whangbo, Magnetic ordering in the frustrated Heisenberg chain system cupric chloride $CuCl_2$, Phys. Rev. B **80**, 024404 (2009).

[39] A. Huq, M. Kirkham, P. F. Peterson, J. P. Hodges, P. S. Whitfield, K. Page, T. Hügle, E. B. Iverson, A. Parizzi, and G. Rennich, POWGEN: rebuild of a third-generation powder diffractometer at the Spallation Neutron Source, J. Appl. Crystallogr. **52**, 1189 (2019).

[40] M. M. J. Treacy, J. M. Newsam, and M. W. Deem, A general recursion method for calculating diffracted intensities from crystals containing planar faults, Proc. R. Soc. Lond. A **433**, 499 (1991).

[41] B. H. Toby and R. B. Von Dreele, *GSAS-II*: the genesis of a modern open-source all purpose crystallography software package, J. Appl. Crystallogr. **46**, 544 (2013).

[42] W. A. Dollase, Correction of intensities for preferred orientation in powder diffractometry: application of the March model, J. Appl. Crystallogr. **19**, 267 (1986).

[43] J. A. Schneeloch, Y. Tao, C. Duan, M. Matsuda, A. A. Aczel, J. A. Fernandez-Baca, G. Xu, J. C. Neuefeind, J. Yang, and

D. Louca, Evolution of the structural transition in $Mo_{1-x}W_xTe_2$, Phys. Rev. B **102**, 054105 (2020).

[44] L. Chen, J.-H. Chung, M. B. Stone, A. I. Kolesnikov, B. Winn, V. O. Garlea, D. L. Abernathy, B. Gao, M. Augustin, E. J. G. Santos, and P. Dai, Magnetic field effect on topological spin excitations in CrI_3, Phys. Rev. X **11**, 031047 (2021).

[45] C. P. Weber, Ultrafast investigation and control of Dirac and Weyl semimetals, J. Appl. Phys. **129**, 070901 (2021).

[46] M. Hagiwara and K. Katsumata, Magnetic properties of anhydrous $CrCl_2$, International conference on magnetism, J. Magn. Magn. Mater. **140-144**, 1665 (1995).

[47] Li. Zhao, T.-L. Hung, C.-C. Li, Y.-Y. Chen, M.-K. Wu, R. K. Kremer, M. G. Banks, A. Simon, M.-H. Whangbo, C. Lee, J. S. Kim, I. Kim, and K. H. Kim, $CuBr_2$ - a new multiferroic material with high critical temperature, Adv. Mater. **24**, 2469 (2012).

[48] C. Lee, J. Liu, M.-H. Whangbo, H.-J. Koo, R. K. Kremer, and A. Simon, Investigation of the spin exchange interactions and the magnetic structure of the high-temperature multiferroic $CuBr_2$, Phys. Rev. B **86**, 060407(R) (2012).

[49] S. Blundell, *Magnetism in Condensed Matter*, Oxford Master Series in Physics (Oxford University Press, Oxford, New York, 2001).

[50] M. Enderle, C. Mukherjee, B. Fåk, R. K. Kremer, J.-M. Broto, H. Rosner, S.-L. Drechsler, J. Richter, J. Malek, A. Prokofiev, W. Assmus, S. Pujol, J.-L. Raggazzoni, H. Rakoto, M. Rheinstädter, and H. M. Rønnow, Quantum helimagnetism of the frustrated spin-$\frac{1}{2}$ chain $LiCuVO_4$, Europhys. Lett. **70**, 237 (2005).

[51] B. J Gibson, R. K Kremer, A. V Prokofiev, W Assmus, and G. J McIntyre, Incommensurate antiferromagnetic order in the $S = \frac{1}{2}$ quantum chain compound $LiCuVO_4$, Proceedings of the third european conference on neutron scattering, Phys. B: Condens. Matter **350**, E253 (2004).

[52] T. Masuda, A. Zheludev, A. Bush, M. Markina, and A. Vasiliev, Competition between Helimagnetism and commensurate quantum spin correlations in $LiCu_2O_2$, Phys. Rev. Lett. **92**, 177201 (2004).

[53] S. Asai, T. Oyama, K. Nawa, A. Nakao, K. Munakata, K. Kuwahara, M. Hagihala, S. Itoh, Z. Hiroi, and T. Masuda, Helical and collinear spin density wave order in the $S = \frac{1}{2}$ one-dimensional frustrated chain compound $NaCuMoO_4(OH)$ investigated by neutron scattering, Phys. Rev. B **101**, 144437 (2020).

[54] B. Willenberg, M. Schäpers, K. C. Rule, S. Süllow, M. Reehuis, H. Ryll, B. Klemke, K. Kiefer, W. Schottenhamel, B. Büchner, B. Ouladdiaf, M. Uhlarz, R. Beyer, J. Wosnitza, and A. U. B. Wolter, Magnetic frustration in a quantum spin chain: The case of linarite $PbCuSO_4(OH)_2$, Phys. Rev. Lett. **108**, 117202 (2012).

[55] J. W. Cable, M. K. Wilkinson, and E. O. Wollan, Neutron diffraction studies of antiferromagnetism in CrF_2 and $CrCl_2$, Phys. Rev. **118**, 950 (1960).

[56] M. Winkelmann, M. Baehr, M. Reehuis, M. Steiner, M. Hagiwara, and K. Katsumata, Structural and magnetic characterization of a new phase of $CrCl_2$, J. Phys. Chem. Solids **58**, 481 (1997).

[57] M. Wu and J. Li, Sliding ferroelectricity in 2D van der Waals materials: Related physics and future opportunities, Proc. Natl. Acad. Sci. USA **118**, e2115703118 (2021).

[58] Q. Song, C. A. Occhialini, E. Ergeçen, B. Ilyas, D. Amoroso, P. Barone, J. Kapeghian, K. Watanabe, T. Taniguchi, A. S. Botana, S. Picozzi, N. Gedik, and R. Comin, Evidence for a single-layer van der Waals multiferroic, Nature (London) **602**, 601 (2022).

[59] Y. Tokura, S. Seki, and N. Nagaosa, Multiferroics of spin origin, Rep. Prog. Phys. **77**, 076501 (2014).

[60] Y. Jiang, Y. Wu, J. Zhang, J. Wei, B. Peng, and C.-W. Qiu, Dilemma in optical identification of single-layer multiferroics, Nature (London) **619**, E40 (2023).

[61] S. Seki, T. Kurumaji, S. Ishiwata, H. Matsui, H. Murakawa, Y. Tokunaga, Y. Kaneko, T. Hasegawa, and Y. Tokura, Cupric chloride $CuCl_2$ as an $S = \frac{1}{2}$ chain multiferroic, Phys. Rev. B **82**, 064424 (2010).

[62] M.-P. Miao, N. Liu, W.-H. Zhang, D.-B. Wang, W. Ji, and Y.-S. Fu, Spin-resolved imaging of atomic-scale helimagnetism in monolayer NiI_2, arXiv:2309.16526.

[63] S. R. Kuindersma, J. P. Sanchez, and C. Haas, Magnetic and structural investigations on NiI_2 and CoI_2, Physica B+C **111**, 231 (1981).

[64] J. M. Carpenter and C.-K. Loong, *Elements of Slow-Neutron Scattering: Basics, Techniques, and Applications* (Cambridge University Press, Cambridge, UK, 2015).

[65] G. Shirane, S. M. Shapiro, and J. M. Tranquada, *Neutron Scattering with a Triple-Axis Spectrometer* (Cambridge University Press, Cambridge, UK, 2002).

[66] A. S Wills, A new protocol for the determination of magnetic structures using simulated annealing and representational analysis (SARA*h*), Phys. B: Condens. Matter **276-278**, 680 (2000).

[67] J. O. Dimmock, Use of symmetry in the determination of magnetic structures, Phys. Rev. **130**, 1337 (1963).